# On the Use of Ocean Surface Doppler Velocity for Oceanic Front Extraction From Chinese Gaofen-3 SAR Data

Kai Sun, Jinsong Chong, *Senior Member, IEEE*, Lijie Diao, Zongze Li, and Xianen Wei

***Abstract*—Oceanic front extraction from synthetic aperture radar (SAR) images is of great significance to the study of marine ecosystems. At present, the methods for oceanic front extraction are usually based on SAR intensity images, which treat oceanic fronts as edge-like features in the SAR images. However, affected by radar parameters and sea state, sometimes, oceanic front signatures may not be clearly visible in the SAR intensity images. Therefore, existing methods are limited. In order to solve this problem, a method combining intensity and Doppler information for oceanic front extraction is proposed. Using Chinese Gaofen-3 single-look complex (SLC) data, three cases where oceanic front signatures are clearly visible, partially visible, and extremely weak in the SAR intensity images are investigated, which demonstrate how the Doppler velocity gradient across a front can be leveraged to enhance the extraction of oceanic fronts from SAR data. The results show that the Doppler data, as supplementary information, not only can complement the oceanic fronts extracted from SAR intensity images, but also can be used as a reference for the oceanic fronts extracted from SAR intensity images.**

***Index Terms*—Chinese Gaofen-3 (GF-3) satellite, oceanic front extraction, surface Doppler velocity, synthetic aperture radar (SAR).**

## I. Introduction

OCEANIC fronts are relatively narrow zones of enhanced horizontal gradients of physical, chemical, optical, and/or biological parameters that separate broader areas with different water masses or different vertical structures [1], [2]. Extraction of oceanic fronts have great significance for studying the transport of heat and mass in the ocean, maintaining a marine ecological balance, as well as exploiting fisheries potential and primary food production.

Synthetic aperture radar (SAR), independent of cloud cover, has the capabilities of day and night, all-weather, high resolution, and wide swath observations. These capabilities enable SAR to be widely used in ocean remote sensing. The interaction of surface waves with currents causes a change in the surface roughness, which also implies a change in normalized radar cross section (NRCS) of the surface [3]. As a result, oceanic fronts are readily detectable by SAR. In the SAR images, oceanic fronts are usually visible as distinct lines, which are clearly brighter or darker than the ambient regions or which separate regions of different mean image intensities [4]. Therefore, the signatures of oceanic fronts in SAR images are always regarded as edge features and oceanic fronts are usually extracted by an edge detection algorithm. Jones *et al.* [5], [6] used an edge detector to identify brightness fronts in RADARSAT-2 SAR images acquired in the vicinity of the Gulf Stream, and then a statistical classification algorithm was applied to discriminate front signatures from horizontal wind shear signatures not associated with oceanic fronts. Wychen *et al.* [7] used RADARSAT-2 and Sentinel-1 SAR images, together with an edge detection tool, to automatically extract ocean features, which include atmospheric boundaries and oceanic fronts. The features were classified as oceanic fronts or atmospheric boundaries by comparing the mean angle of the local wind along the entire length of the feature with the orientation of the feature.

The methods mentioned above are based on SAR intensity images. However, the capability of SAR to detect oceanic fronts is related to radar parameters, such as frequency [8], [9], polarization [8], [9], incidence angle [3], and look direction [10], and is also influenced by wind [11], [12] and current [10]. Therefore, in some cases, the signature of oceanic fronts is extremely weak in the SAR intensity image. As a consequence, oceanic front extraction methods based on the SAR intensity image are no longer appropriate.

The significant surface velocity gradient across a front is an essential feature of oceanic fronts [13]–[15]. The motion of sea surface scatterers induced by frontal current gradient due to wave-current interaction is recorded in the SAR Doppler. Chapron *et al.* [16] pioneered the method to retrieve the surface Doppler velocity from single antenna satellite SAR measurements and pointed out that the Doppler velocity contains contributions from ocean surface motion induced by wind and currents. Subsequent studies have shown that although the Doppler velocity is not a direct surface current measurement, the use of Doppler observations can help to derive new and innovative estimates of the mesoscale dynamics [17]. With particular interest in the Gulf Stream, Biron *et al.* [18] demonstrated the capability of Doppler velocity to extract the position of strong

Manuscript received December 29, 2021; revised February 12, 2022 and March 13, 2022; accepted March 22, 2022. Date of publication March 25, 2022; date of current version April 13, 2022. *(Corresponding author: Jinsong Chong.)*

Kai Sun, Jinsong Chong, Lijie Diao, Zongze Li, and Xianen Wei are with the National Key Laboratory of Microwave Imaging Technology, Aerospace Information Research Institute, Chinese Academy of Sciences, Beijing 100190, China, and also with the School of Electronic, Electrical, and Communication Engineering, University of Chinese Academy of Sciences, Beijing 100049, China (e-mail: sunkai181@mails.ucas.ac.cn; lily@mail.ie.ac.cn; diaolijie21@mails.ucas.ac.cn; lizongze20@mails.ucas.ac.cn; weixianen20@mails.ucas.ac.cn).

Digital Object Identifier 10.1109/JSTARS.2022.3162445

currents using Sentinel-1 radial velocity products. However, the resolution of the Doppler velocity images is coarser than that of the SAR intensity images, which may lead to a deviation of the extracted position of the front. Moreover, the capability of Doppler techniques to extract ocean surface currents is affected by both the direction and magnitude of the wind and currents velocities because only one component velocity (i.e., radial velocity) can be captured.

In this article, a method combining intensity and Doppler information for oceanic front extraction from Chinese Gaofen-3 (GF-3) single-look complex (SLC) data is proposed. The method takes benefit of the high resolution of the SAR intensity images and takes benefit of the good performance of Doppler in capturing the velocity gradient across the front. First, the Doppler velocity gradient of oceanic fronts is derived, and the least squares technique is applied to extract an oceanic front. Then, the oceanic front is extracted from the SAR intensity image. Finally, a fusion algorithm is utilized after a decision. The performance of the method is verified by application to three cases that oceanic front signatures are clearly visible, partially visible, and extremely weak in the SAR intensity images.

The rest of this article is organized as follows. Section II details the methodology, followed by the case studies in Section III. Section IV presents a brief discussion. Finally, Section V concludes this article.

## II. Methodology

The flow chart of the proposed method in this article is shown in Fig. 1. The input is GF-3 SLC data. As illustrated in Fig. 1, the process consists of four parts: ocean surface Doppler velocity estimation, oceanic front extraction from ocean surface Doppler velocity gradient, oceanic front extraction from SAR intensity images, and decision fusion. The abovementioned four parts will be detailed as follows.

### A. Ocean Surface Doppler Velocity Estimation

The received signal experiences a Doppler shift because of the relative motion of the sensor and the target [19]. Doppler shift is the key capability of SAR to measure velocity, which is widely used to separate moving targets from stationary clutter [20]. As the beam has its maximum gain along its central axis or boresight, the peak modulation occurs at the time that the beam center crosses the target. The Doppler frequency at this time is the azimuth center frequency of the data, and is referred to as the "Doppler centroid" [19]. The Doppler centroid $f_{Dc}$ can be estimated from the SLC data, the predicted Doppler shift $f_{Dp}$ arising from the relative of the satellite and rotating earth, and a Doppler centroid anomaly is defined by [21]

$$f_{Dca} \equiv f_{Dc} - f_{Dp}. \tag{1}$$

A geophysical Doppler shift relates to the Doppler centroid anomaly by [21]

$$f_{\text{phys}} = f_{Dca} - f_{\text{err}} \tag{2}$$

where $f_{\text{err}}$ accounts for the estimation errors of both $f_{Dca}$ and $f_{Dp}$, antenna electronic mispointing, residual error coming from imperfect prediction of the nongeophysical terms or other unknown biases. $f_{\text{phys}}$ should be zero for a surface at rest with respect to the earth. For the dynamic sea surface, however, the geophysical Doppler shift relates to the motion information of both current and surface scatterers, converted to ocean surface Doppler velocity

$$v_d = -\frac{\pi f_{\text{phys}}}{k_e \sin\theta_I} \tag{3}$$

where $k_e$ is the electromagnetic wavenumber and $\theta_I$ is the angle of incidence of the radar beam relative to the normal to the surface. The positive Doppler velocity is directed toward the SAR look direction, and the negative Doppler velocity is directed away from the SAR look direction.

*1) Doppler Centroid $f_{Dc}$ Estimation:* For the dynamic sea surface, the motion of each part is different, which results in a different Doppler shift. Therefore, SLC data are divided into $M \times N$ subblocks of equal size along the azimuth direction and range direction, and the Doppler centroid of each subblock is estimated. The size of each subblock is $Na \times Nr$, where $Na$ and $Nr$ represent the number of azimuth and range pixels, respectively. The selection of $Na$ and $Nr$ depends on the relationship between the Doppler pixel spacing and the SAR-image pixel spacing. $M$ and $N$ are the ratios of the SLC data size and the subblock size in the azimuth and range directions, respectively, rounded down. In this article, a correlation Doppler estimator method, proposed by Madsen [22], is used to estimate the Doppler centroid. The method starts from the time domain and utilizes the Fourier transform relationship between the signal power spectrum and the correlation function. The Doppler centroid is estimated by the phase difference of radar data. The Doppler centroid of each subblock is

$$f_{Dc} = \frac{\text{PRF}}{2\pi} \arg\left(\overline{C(\eta,\tau)}\right) \tag{4}$$

where operator $\arg(\cdot)$ denotes the argument of a complex number, $C(\eta,\tau)$ is the average autocorrelation coefficient, $\eta$ is the SAR azimuth time, $\tau$ is the SAR range time. $PRF$ is the SAR pulse repetition frequency, and the autocorrelation coefficient $C(\eta,\tau)$ is as follows:

$$C(\eta,\tau) = \sum_{\eta} s(\eta,\tau)\, s^*(\eta+\Delta\eta,\tau) \tag{5}$$

where $s(\eta,\tau)$ is the SAR signal in the time domain, $*$ indicates a complex-valued conjugate, and $\Delta\eta = 1/PRF$. The average autocorrelation coefficient $\overline{C(\eta,\tau)}$ is calculated as follows:

$$\overline{C(\eta,\tau)} = \frac{1}{Nr}\sum_{r=1}^{Nr} C(\eta,\tau_r). \tag{6}$$

Combining (4)–(6), the Doppler centroid of each subblock can be written as

$$f_{Dc} = \frac{\text{PRF}}{2\pi}\frac{1}{Nr}\arg\left\{\sum_{r=1}^{Nr}\sum_{\eta} s(\eta,\tau_r)\, s^*(\eta+\Delta\eta,\tau_r)\right\}. \tag{7}$$

It should be noted that due to the earth's rotation, the Doppler centroid varies over the orbit, while the data are sampled with the pulse-repetition frequency, and an ambiguity about the correct $PRF$ band remains [23]. However, the GF-3 spacecraft operation follows a zero-Doppler attitude steering mode, which is designed to reduce the Doppler centroid of the stationary target to a theoretical 0 Hz. In addition, since the

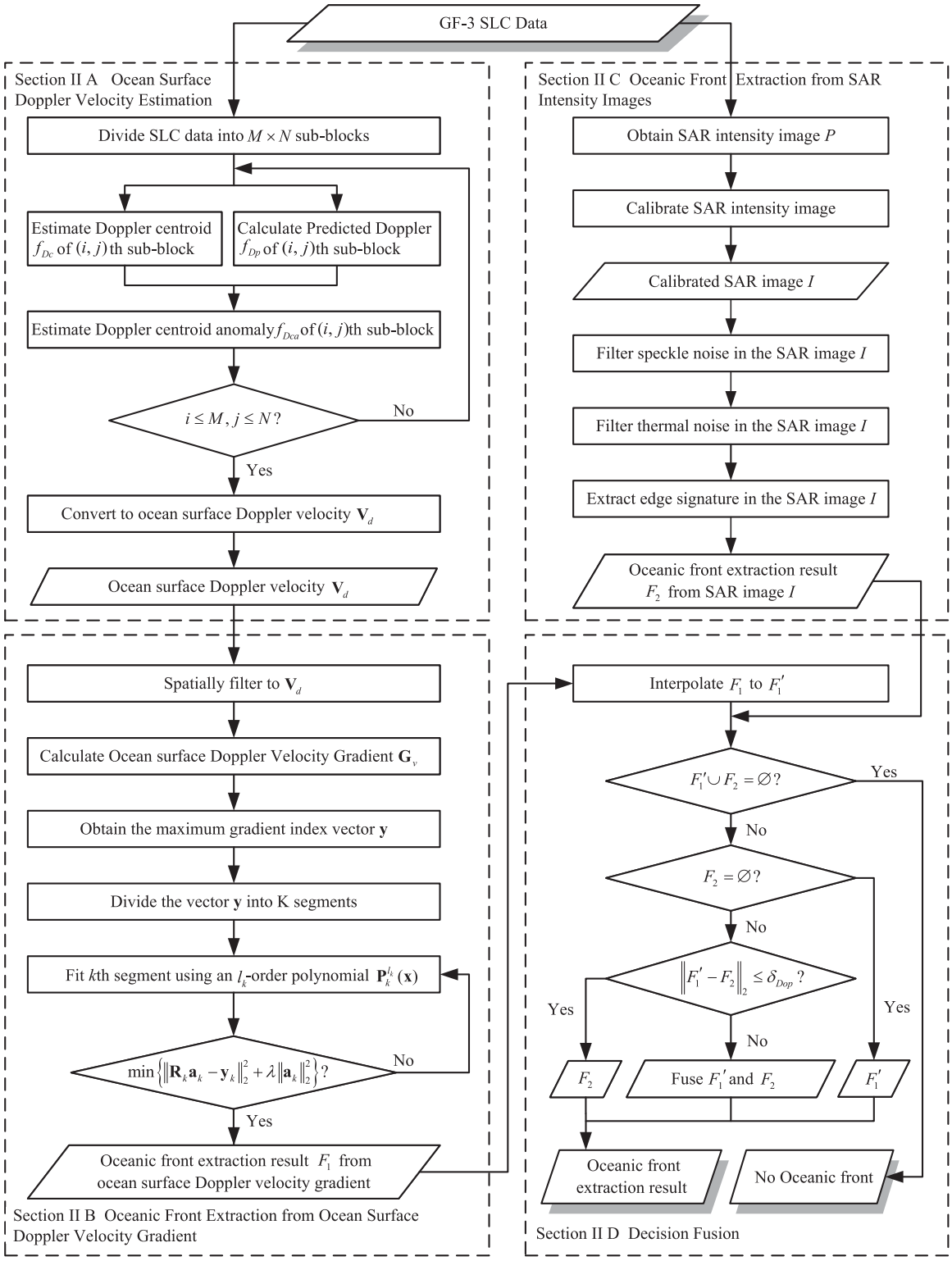


Fig. 1. Flowchart of the proposed methodology. The symbols and various expressions will be further explained in the rest of Section II.

Doppler velocity of the ocean surface current usually does not exceed 2 m/s, the Doppler shift induced by a current lies within $[-PRF, PRF)$. Therefore, $PRF$-ambiguity resolving is not necessary in this article.

*2) Predicted Doppler $f_{Dp}$ Calculation:* The systematic factors affecting the predicted Doppler $f_{Dp}$ can be summarized as the satellite orbit geometry, radar beam pointing, and the intersection point of the beam with the rotating surface. The predicted Doppler is a function of range and is mainly related to

the satellite yaw, pitch, and roll angles. The predicted Doppler is given by [21], [24]

$$f_{Dp} = \frac{2v_{sc}}{\lambda}\sin\gamma\cos\alpha \times \left[1-(\omega_e/\omega)\left(\varepsilon\cos\beta\sin\psi\tan\alpha+\cos\psi\right)\right] \quad (8)$$

where the first term represents a Doppler component arising from the spacecraft motion, and the remaining two terms come from earth rotation. Specifically, $v_{sc}$ is the magnitude of the spacecraft velocity along its orbital path, $\lambda$ is the radar wavelength, $\gamma$ is the elevation angle of the radar beam, $\alpha$ is the angle between the range elevation plane and the spacecraft orbital plane (yaw), $\omega_e$ is the angular rate of the earth's rotation, $\omega$ is the spacecraft orbital rotation angular rate, $\varepsilon$ describes whether the radar is looking to the right (+1) or left ($-1$) of the orbital velocity vector, $\beta$ is the argument of latitude, defined as the angle measured between the ascending node and the spacecraft position in the orbit plane from the center of the earth, $\psi$ is the inclination of the spacecraft orbital plane.

In terms of GF-3 spacecraft, zero-Doppler attitude steering has compensated for the Doppler shift caused by the earth's rotation, in this way, $f_{Dp}$ is only due to pointing inaccuracy, orbit variation errors, variations in terrain height, or implementation approximations. From GF-3 auxiliary data, the predicted Doppler can be calculated following the equation

$$f_{Dp} = \begin{bmatrix} d_0 & d_1 & d_2 & d_3 & d_4 \end{bmatrix} \begin{bmatrix} 1 \\ (t_s-t_0) \\ (t_s-t_0)^2 \\ (t_s-t_0)^3 \\ (t_s-t_0)^4 \end{bmatrix} \quad (9)$$

where $d_i (i=1,2,3,4)$ are the Doppler coefficients, $t_s$ is the two-way range time, and $t_0$ is the reference time.

### B. Oceanic Front Extraction From Ocean Surface Doppler Velocity Gradient

Since velocity varies with different local sea surface areas, and the coastal area is more likely to cause discontinuities in the Doppler estimation results, the ocean surface Doppler velocity $\mathbf{V}_d$ is first spatially filtered to facilitate subsequent processing. Calculating the gradient of filtered Doppler velocity, the ocean surface Doppler velocity gradient $\mathbf{G}_v$ is obtained.

The Doppler velocity is sensitive to direction, thus the Doppler velocity gradient $\mathbf{G}_v$ is also related to direction. Oceanic front velocity gradients can be acquired except for the case where the direction of the oceanic front is aligned with azimuthal direction. The Doppler velocity increases with radially directed front velocity as well as increasing front velocity. A maximum Doppler velocity corresponds to the case where the front is strong and roughly aligned with range direction. In this case, a maximum Doppler velocity gradient may be also obtained.

Let $r$ and $s$ denote the index of the azimuth and range directions, respectively, and the azimuth index corresponding to the maximum magnitude of all elements of each range cell of $\mathbf{G}_v$ is taken. Then, the vector $\mathbf{y} \in \mathbb{R}^{N-1}$ is obtained. The values of $\mathbf{y}$ can be expressed as

$$y_s = \arg\max_r \left(\|\mathbf{G}_v(r,s)\|_2\right) \quad \begin{matrix} r=1,2,\ldots,M-1 \\ s=1,2,\ldots,N-1. \end{matrix} \quad (10)$$

After taking the derivative of the vector $\mathbf{y}$ with respect to $s$, the vector $\mathbf{y}$ is then divided into $K(1 \le K \le N-1)$ segments according to the fact that the oceanic front is continuous. For the $k$th segment $\mathbf{y}_k \in \mathbb{R}^{S_k}$, $S_k$ satisfies $\sum_{k=1}^{K} S_k = N-1$. An $l_k-$order polynomial $\mathbf{p}_k^{l_k}(\mathbf{x}) = \mathbf{R}_k\mathbf{a}_k$ is utilized to fit each vector $\mathbf{y}_k$, where $\mathbf{x} = [x_1, x_2, \ldots, x_p, \ldots, x_{S_k}]^\top$, $x_p = s$, $\mathbf{R}_k \in \mathbb{R}^{S_k \times (l_k+1)}$. The polynomial coefficients $\mathbf{a}_k$ can be obtained by solving the $L_2$ regularization problem

$$\hat{\mathbf{a}}_k = \arg\min_{\mathbf{a}_k} \left\{ \|\mathbf{R}_k\mathbf{a}_k - \mathbf{y}_k\|_2^2 + \lambda \|\mathbf{a}_k\|_2^2 \right\} \quad (11)$$

where $\lambda$ is the regularization parameter of the term $\|\mathbf{a}_k\|_2$, and $\|\mathbf{a}_k\|_2$ can be expressed as follows

$$\|\mathbf{a}_k\|_2 = \left( \sum_{\ell=1}^{l_k+1} |\mathbf{a}_k(\ell)|^2 \right)^{\frac{1}{2}}. \quad (12)$$

The estimates of polynomial coefficients $\hat{\mathbf{a}}_k$ can be expressed as follows:

$$\hat{\mathbf{a}}_k = (\mathbf{R}_k{}^\top\mathbf{R}_k - \lambda\mathbf{I})^{-1}\mathbf{R}_k{}^\top\mathbf{y}_k. \quad (13)$$

In this way, the polynomial $\mathbf{p}_k^{l_k}(\mathbf{x})$ can be determined. All the points $(x_p, \mathbf{p}_k^{l_k}(x_p))$ that satisfy $\left\|\mathbf{p}_k^{l_k}(\mathbf{x}) - \mathbf{y}\right\|_2 \le 2\delta_{Dop}$ (where $\delta_{Dop}$ is the Doppler resolution) form a set $F_1$, as the result of oceanic front extraction from ocean surface Doppler velocity gradient.

### C. Oceanic Front Extraction From SAR Intensity Images

The magnitude of the input GF-3 SLC data is taken to obtain the SAR intensity image. In order to accurately reflect the scattering characteristics of oceanic fronts, the SAR intensity image is radiometrically calibrated first. For GF-3 SAR data, the NRCS can be expressed as

$$\sigma^0 = 10\lg\left[P^2(QualifyValue/32767)^2\right] - K_{dB} \quad (14)$$

where $P^2$ is the intensity of SAR images, $QualifyValue$ is the quantized value of data, and $K_{dB}$ is the calibration constant.

Then, the speckle noise and thermal noise in the SAR intensity image are filtered to reduce the influence of noise on subsequent processing to improve the extraction accuracy. Finally, the gradient at each pixel $(x,y)$ of the calibrated SAR intensity image $I$ is calculated.

$$\nabla I = [g_x \;\; g_y]^\top = \left[\frac{\partial\sigma^0}{\partial x} \;\; \frac{\partial\sigma^0}{\partial y}\right]^\top. \quad (15)$$

The gradient vector indicating the magnitude $M(x,y)$ and direction $\alpha(x,y)$ of the maximum rate of change at pixel $(x,y)$ in the SAR intensity image are given by

$$M(x,y) = \|\nabla I\|_2 \quad (16)$$

$$\alpha(x,y) = \arctan\left(g_y/g_x\right). \quad (17)$$

According to $M(x,y)$ and $\alpha(x,y)$, points $(x_0,y_0)$ in the SAR intensity image are extracted, and all the points form a set $F_2$ as the result of oceanic front extraction from SAR intensity images.

TABLE I
SCENES DISCUSSED IN CASE STUDIES

| Case | Imaging Time [UTC] | SAR Mode | Polarization | Orbit | Swath [km] | Incidence Angle [deg] |
|---|---|---|---|---|---|---|
| 1 | 2020-02-25 21:37:52 | QPSI | VV | Descending | 30 | 35.45-37.12 |
| 2 | 2020-11-24 21:43:15 | FSII | HH | Descending | 100 | 37.22-43.39 |
| 3 | 2021-04-26 21:11:54 | FSI | VV | Descending | 50 | 43.12-45.72 |

### *D. Decision Fusion*

In order to facilitate the decision of oceanic front extraction result from ocean surface Doppler velocity gradient $F_1$ and oceanic front extraction result from SAR intensity images $F_2$, for each point $(x_p, \mathbf{p}_k^{l_k}(x_p))$ in $F_1$, the corresponding point $(x_q, y_q)$ in the SAR intensity image is

$$x_q = \left\lfloor Na \times \ x_p - \frac{Na}{2} \right\rfloor$$
$$y_q = \left\lfloor Nr \times \ y_p - \frac{Nr}{2} \right\rfloor, \ y_p = \mathbf{p}_k^{l_k}(x_p) \tag{18}$$

where $\lfloor \cdot \rfloor$ represents rounding down. Since the Doppler velocity gradient has a coarser resolution and fewer pixels than that of the SAR intensity images, it is interpolated to the same resolution as the SAR intensity images, the interpolated oceanic front extraction result is recorded as ${F_1}'$.

The decision of oceanic front extraction results is taken according to the three different manifestations of oceanic front signature in the SAR intensity images. For the case in which the oceanic front signature is clearly visible in SAR intensity images, (i.e., $\|{F_1}' - F_2\|_2 \leq \delta_{Dop}$), $F_2$ is used as the oceanic front extraction result. For the case in which the oceanic front signature is partially visible in the SAR intensity images, ${F_1}'$ and $F_2$ are fused as the oceanic front extraction result $F$

$$F = \rho F_1' + (1 - \rho) F_2 \tag{19}$$

where $\rho$ stands for the weight coefficient, and the value of $\rho$ is determined by

$$\rho = \begin{cases} 1 & \text{SNR} < th \\ 0 & \text{others} \end{cases} \tag{20}$$

where $SNR$ is the signal-to-noise ratio given by the following equation, and $th$ is the threshold, which depends on the actual data and is theoretically 0:

$$\text{SNR} = 10 \log 10 \frac{E\left\{\left|\sigma_F^0\right|^2\right\}}{E\left\{\left|\sigma_B^0\right|^2\right\}} \tag{21}$$

where $E\{\cdot\}$ stands for the expectation operator, $\sigma_F^0$ is the NRCS of the SAR intenstiy images at the location of an oceanic front, and $\sigma_B^0$ is the NRCS of the uniform ocean background. For the case in which the oceanic front signature is extremely weak in the SAR intensity images, that is, $F_2 = \emptyset$, $\emptyset$ denotes an empty set, ${F_1}'$ is used as the final result.

## III. CASE STUDIES

In this section, three case studies of oceanic front extraction from GF-3 SLC data carried out using proposed method are presented. GF-3, launched on August 10, 2016, is the first Chinese C-band multipolarized SAR satellite with the highest resolution of one meter for marine surveillance and monitoring. GF-3 SAR has 12 imaging modes and good ocean and coastal monitoring capabilities [25]–[28]. The scenes of GF-3 data were selected (listed in Table I) because they highlight three distinct cases: 1) the oceanic front signature is clearly visible in the SAR intensity image, 2) the oceanic front signature is partially visible in the SAR intensity images, and 3) the oceanic front signature is extremely weak in the SAR intensity images.

### *A. Case 1: Oceanic Front Signature is Clearly Visible in the SAR Intensity Images*

*1) Results:* Fig. 2(a) shows the GF-3 image that was acquired on February 25, 2020 at 21:37:52 UTC (descending pass, VV polarization), with the center of the image being located at 125.91 °E, 27.98 °N. The arrows indicate the azimuth (A) and range (R) directions. As shown in Fig. 2(a), a line with sharp gradient of NRCS is approximately distributed along the range direction at the lower middle part of the SAR image, which is consistent with the signature of the oceanic front in the SAR images. Furthermore, the oceanic front can be judged as the Kuroshio front according to its geographical location. Fig. 2(b) represents the estimated ocean surface Doppler velocity, as can be seen, the direction of the Doppler velocity is roughly aligned with the main direction of propagation of the Kuroshio. Fig. 2(c) shows the Doppler velocity gradient, where the solid black line indicates the oceanic front extracted from the Doppler velocity gradient. Fig. 2(d) is the oceanic front extraction result. The solid red line indicates the oceanic front extracted from the Doppler velocity gradient, and the solid blue line indicates that extracted from the SAR intensity image.

*2) Interpretation:* To clearly compare and analyze the oceanic front extraction result from the SAR intensity image and that from the Doppler velocity gradient, we take the SAR image transect shown by the solid white line in Fig. 2(d) and its corresponding Doppler velocity gradient transect. The transect is taken because the distance between the oceanic front extracted from the ocean surface Doppler velocity gradient and that extracted from SAR intensity image is farthest. We calculate the SAR image contrast and compare it with the Doppler velocity gradient along the transect, the equation of SAR image contrast $CR$ is expressed as

$$CR = \left|(I_t - \bar{I}_t)/\bar{I}_t\right| \tag{22}$$

where $I_t$ is the intensity of SAR image along the transect, and $\bar{I}_t$ is the average intensity of SAR image along the transect. The purpose of taking the absolute value is to keep the $CR$ positive at the location of the oceanic front, regardless of whether the oceanic front is a bright line or a dark line in the SAR image.

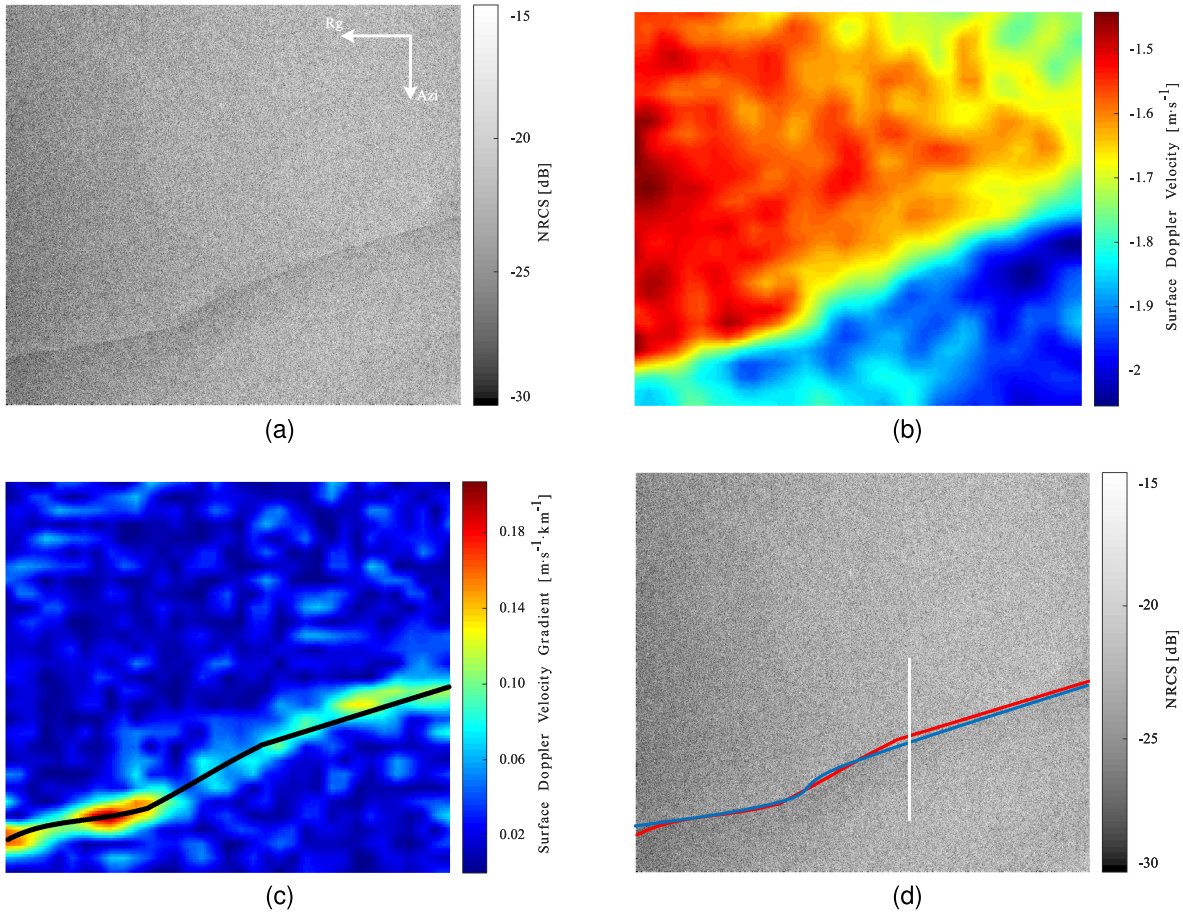


Fig. 2. Case of GF-3 QPSI mode data acquired on February 25, 2020 at 21:37:52 UTC (descending, VV polarization). (a) SAR intensity image. The azimuth (A) and range (R) directions are indicated by arrows. (b) Estimated Doppler velocity. (c) Doppler velocity gradient with the extracted oceanic front (solid black line) superimposed. (d) Oceanic front extraction results, where the solid red line and the solid blue line indicate the oceanic front extracted from the Doppler velocity gradient and SAR intensity image, respectively. The solid white line indicates the transect for the analysis.

The positions of the oceanic front in the SAR intensity and that in the Doppler velocity gradient are determined by the highest SAR image contrast variation peak and the highest Doppler velocity variation peak along the transect, respectively.

Fig. 3 illustrates a comparison of variations of SAR image contrast and the Doppler velocity gradient along the transect shown by the white line in Fig. 2(d), where the red and the blue lines indicate the variation of the Doppler velocity gradient and the variation of SAR image contrast along the transect, respectively. It can be seen that the oceanic front corresponds to the Doppler velocity gradient variation, located at 7.92 km along the transect, exceeding the ambient Doppler velocity gradient by two times. The variation of SAR image contrast also reaches its highest peak at 8.45 km along the transect, with a distance of 0.53 km with respect to the position of oceanic front extracted from the Doppler velocity gradient. The variations of NRCS are affected by both wind and wave amplitude and direction, which could offset the local positions of NRCS maxima [29]. The Doppler velocity relates to a spatial mean of the range velocity component weighted by the surface local NRCS, which is a result of the line-of-sight velocities of all surface scattering elements, including Bragg resonance waves, specular

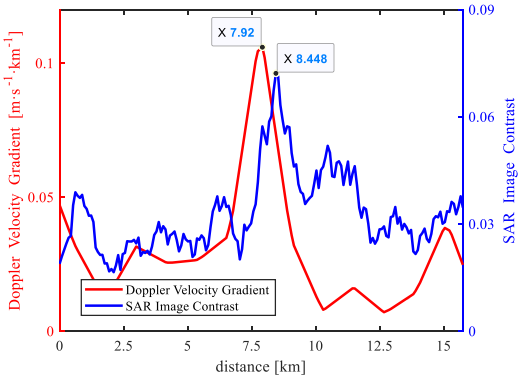


Fig. 3. Comparison of variations of SAR image contrast and the Doppler velocity gradient along the transect shown by the white line in Fig. 2(d), where the blue line indicates the variation of SAR image contrast along the transect, and the red line indicates the variation of the Doppler velocity gradient along the transect.

facets, and breaking waves, advected by and interacting with the underlying surface currents [16], [17]. Therefore, we expect the Doppler variation peak and SAR image contrast variation peak to be located close to each other but not necessarily in

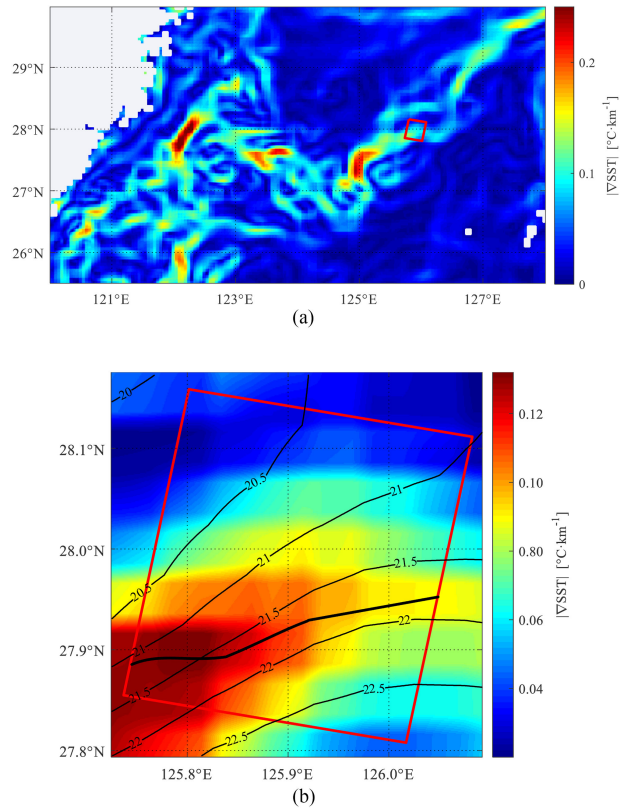


Fig. 4. SST gradient derived from the SST data acquired on February 25, 2020 at 12:00:00 UTC, where the red box refers to the location of the GF-3 image. (b) An enlarged image at the location of the SAR image with the extracted oceanic front from SAR (thick black line) superimposed, where the overlaid thin black lines represent the isotherms.

the same place. The result is promising, which implies that the oceanic front extracted from the Doppler velocity gradient can be used as a reference for the oceanic front extracted from the SAR intensity images.

In this article, the sea surface temperature (SST) gradient is utilized as a reference for the oceanic front extraction results. The SST gradient is derived from SST data. The SST data are acquired from the operational sea surface temperature and ice analysis system, which produces high-resolution analysis and intercomparison products for the SST of the global ocean from satellite and *in situ* data [30].

Fig. 4(a) shows the SST gradient derived from the SST data acquired on February 25, 2020 at 12:00:00 UTC, where the red box indicates the location of the GF-3 image. Fig. 4(a) and (b) shows that the Kuroshio flows through the SAR image coverage area from the south to the north and an enlarged image with the extracted oceanic front from SAR SLC data. As shown in Fig. 4(b), the oceanic front extraction result falls within 21 °C–22 °C isotherms with a strong SST gradient of approximately 0.08–0.15 °C/km, which is due to the front being the strong western boundary warm current Kuroshio. Fig. 4 shows that in the case where the oceanic front signature is clearly visible in the SAR intensity images, oceanic fronts extracted from both the SAR intensity image and the ocean surface Doppler velocity are credible.

### *B. Case 2: Oceanic Front Signature is Partially Visible in the SAR Intensity Images*

*1) Results:* Fig. 5(a) shows the GF-3 image that was acquired on November 24, 2020 at 21:43:15 UTC (descending pass, HH polarization), with the center of the image being located at 123.16 °E, 22.39 °N. The azimuth (A) and range (R) directions are indicated by arrows. The dotted red box refers to the area where the oceanic front signature is invisible in the SAR intensity image. Fig. 5(b) shows the estimated ocean surface Doppler velocity, where the dotted black box refers to the area corresponding to the dotted red box in the SAR intensity image. Fig. 5(c) shows the Doppler velocity gradient with the extracted oceanic front (black line) superimposed, where the solid black line indicates that the signature of oceanic front is visible in the SAR intensity image, and the dashed black line indicates that the signature of oceanic front is invisible in the SAR intensity image. Fig. 5(d) shows the oceanic front extraction results. The solid blue line indicates the oceanic front extracted from the SAR intensity image, and the red line indicates that extracted from the Doppler velocity gradient. The solid red line indicates the extraction result of the oceanic front signature visible in the SAR image, and the dashed red line indicates the extraction result of the oceanic front signature invisible in the SAR image.

In Fig. 5(a), two oceanic fronts can be observed. They have the same orientation that is approximately distributed along the diagonal of the image and are disconnected at four-fifths of the range direction [see dotted red box in Fig. 5(a)]. It is worth noting that the continuous Doppler velocity boundary shown in the dotted black box in Fig. 5(b) exactly corresponds to the red dotted box in Fig. 5(a), which implies that the two oceanic fronts in Fig. 5(a) are actually the same one. According to the estimated Doppler velocity, it is reasonable to assume that the front in the red box in Fig. 5(a) is approximately distributed along the range direction, which may lead to it being invisible in the SAR intensity image. Comparing Fig. 5(a) with (c), it is found that the invisible part of the oceanic front signature in the SAR intensity image [see red dotted box in Fig. 5(a)] can be extracted from the Doppler velocity gradient [see dashed black line in Fig. 5(c)]. Since the Doppler is insensitive to azimuthal velocity, when the oceanic front is approximately parallel to the azimuth direction, the Doppler velocity signature is relatively weak, which results in some nonuniform sea surface features easily interfering with the Doppler velocity gradient arising from the oceanic fronts, as shown in the red dotted box in Fig. 5(c). This artifact can be filtered out using the continuity condition of oceanic fronts. Fig. 5(d) shows the oceanic front extracted from the Doppler velocity gradient and that extracted from the SAR intensity image can be well fused.

*2) Interpretation:* Three SAR image transects shown by the solid white lines in Fig. 5(d) and their corresponding Doppler velocity gradient transects are taken. As shown in Fig. 5(a) and (d), the signature of oceanic front intercepted by transect 1 is visible only in the SAR intensity image, the signature of oceanic front intercepted by transect 2 is visible only in the Doppler velocity gradient image, and the signature of oceanic front intercepted by transect 3 is visible both in the SAR intensity image and the Doppler velocity gradient image.

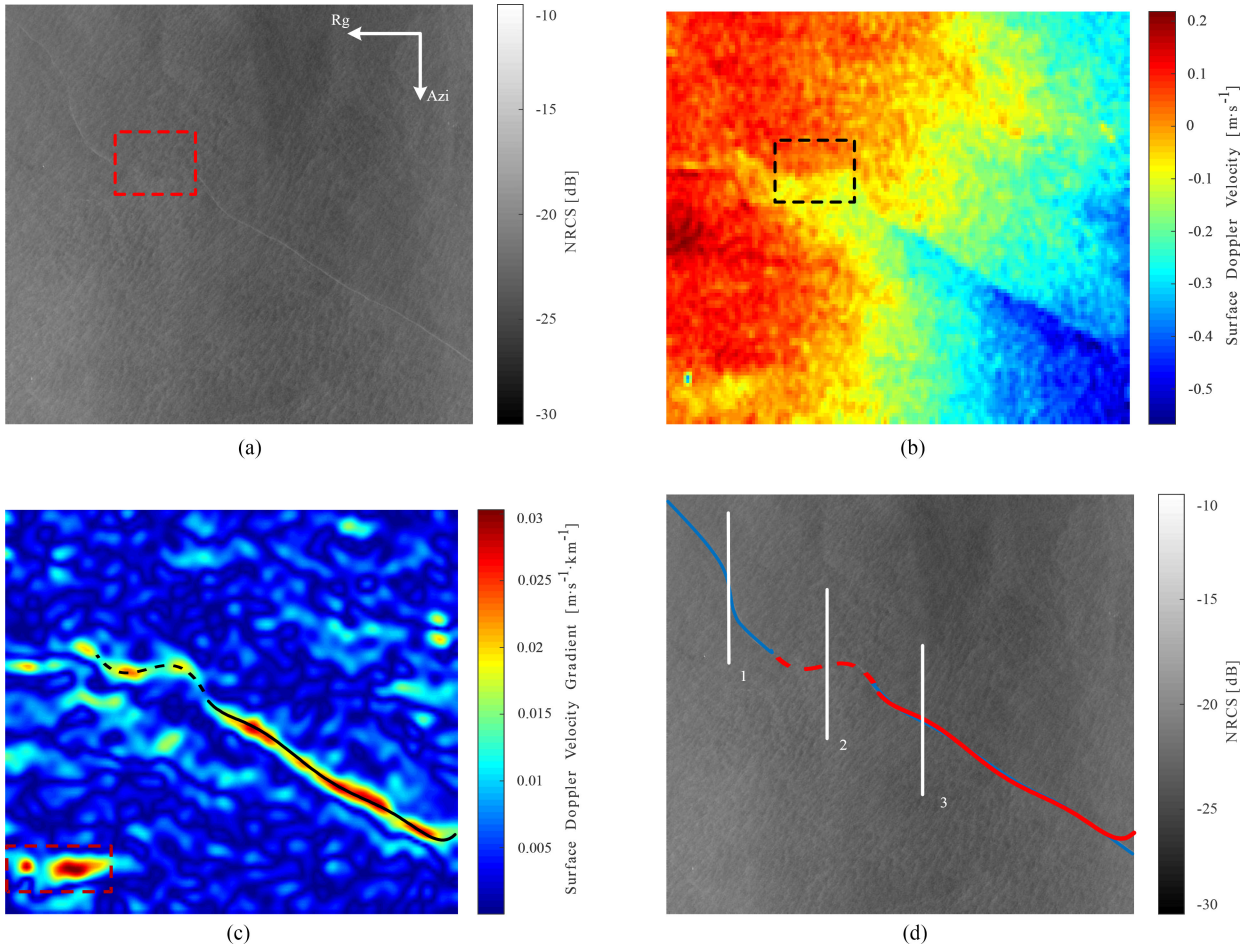


Fig. 5. Case of GF-3 FSII mode data acquired on November 24, 2020 at 21:43:15 UTC (descending pass, HH polarization). (a) SAR intensity image. The azimuth (A) and range (R) directions are indicated by arrows. (b) Estimated Doppler velocity. (c) Doppler velocity gradient with the extracted oceanic front (solid black line) superimposed. (d) Oceanic front extraction results. The solid blue line is the oceanic front extracted from the SAR intensity image, and the red line is that extracted from the Doppler velocity gradient. The solid red line indicates the extraction result of the oceanic front signature visible in the SAR image, and the dashed red line indicates the extraction result of the oceanic front signature invisible in the SAR image. The solid white line indicates the transect for the analysis.

Fig. 6(a) illustrates a comparison of variations of SAR image contrast and the Doppler velocity gradient along transect 1 shown in Fig. 5(d), where the red and the blue lines indicate the variation of the Doppler velocity gradient and the variation of SAR image contrast along transect 1, respectively. As shown in Fig. 6(a), the variation of SAR image contrast has a highest peak located at 23.59 km along transect 1, while the Doppler velocity gradient does not have a significant peak. This is because the oceanic front is approximately parallel to the azimuth direction, and the Doppler velocity signature is relatively weak, which results in the Doppler velocity gradient arising from the oceanic front not being significant.

A comparison of variations of SAR image contrast and the Doppler velocity gradient along transect 2 in Fig. 5(d) is presented in Fig. 6(b), where the red and the blue lines indicate the variation of the Doppler velocity gradient and the variation of SAR image contrast along the transect 2, respectively. As shown in Fig. 6(b), the variation of the Doppler velocity gradient reaches its peak at 23.49 km along transect 2, the position of the peak corresponds to the red dotted line intercepted by transect 2 in Fig. 5(d), while the variation of SAR image contrast is relatively uniform, without a significant peak. In addition, the oceanic front extracted from the Doppler velocity gradient and that extracted from the SAR intensity image can be well connected [see Fig. 5(d)], which implies that the oceanic front extracted from the Doppler is effective to supplement that extracted from SAR intensity in the case where the oceanic front signature is not visible in the SAR intensity image.

Fig. 6(c) exhibits a comparison of variations of SAR image contrast and the Doppler velocity gradient along transect 3 shown in Fig. 5(d), where the red and the blue lines indicate the variation of the Doppler velocity gradient and the variation of SAR image contrast along transect 3, respectively. The variation of SAR image contrast and the Doppler velocity gradient have peaks located at 23.87 km and 23.40 km along transect 3, respectively, with a distance of 0.47 km. The result is promising and is consistent with that shown in Fig. 3.

Fig. 7(a) shows the SST gradient derived from the SST data acquired on November 24, 2020 at 12:00:00 UTC, where the red box refers to the location of the GF-3 image. A linear strong SST gradient in the area covered by SAR image can

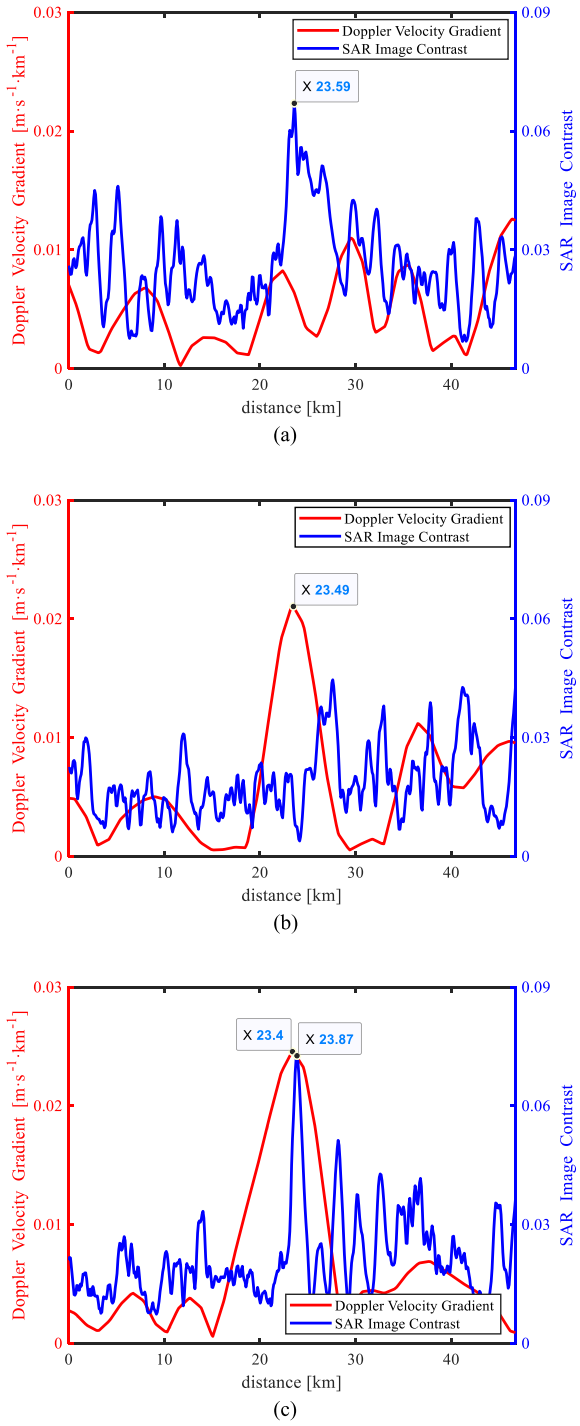


Fig. 6. Comparison of variations of SAR image contrast and the Doppler velocity gradient along (a) transect 1, (b) transect 2, and (c) transect 3 shown in Fig. 5(d). The red and the blue lines indicate the variation of the Doppler velocity gradient and the variation of SAR image contrast along three transects, respectively.

be observed. Fig. 7(b) shows an SST gradient enlargement in the study area with the oceanic front extracted from SAR (thick black line) overlaid on, where the thin black solid line indicates the isotherms. As shown in Fig. 7(b), the oceanic front extracted from SAR exhibits a linear feature similar to the SST gradient, which demonstrates that in the case where

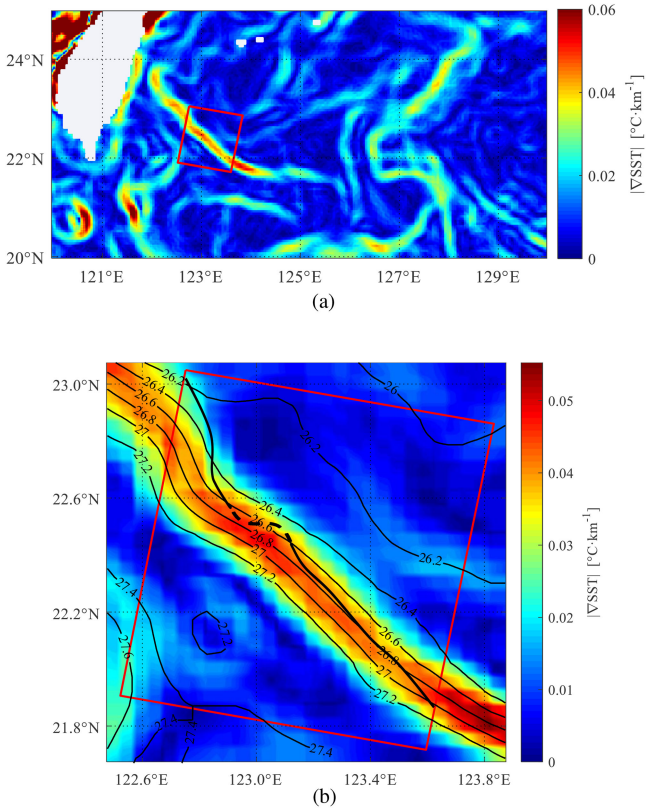


Fig. 7. (a) SST gradient derived from the SST data acquired on November 24, 2020 at 12:00:00 UTC, where the red box refers to the location of the GF-3 image. (b) An enlarged image at the location of the SAR image with the extracted oceanic fronts from SAR (thick black line) superimposed, where the overlaid thin black lines represent the isotherms.

the signature of oceanic front is partially visible in the SAR intensity images, the oceanic fronts extracted from both the SAR intensity image and the ocean surface Doppler velocity are credible.

### *C. Case 3: Oceanic Front Signature is Extremely Weak in the SAR Intensity Images*

*1) Results:* Fig. 8(a) shows the GF-3 image that was acquired on April 26, 2021 at 21:11:54 UTC (descending pass, VV polarization), with the center of the image being located at 130.58 °E, 24.44 °N. The arrows indicate the azimuth (A) and range (R) directions. Fig. 8(b) shows the estimated ocean surface Doppler velocity. In Fig. 8(a), the oceanic front signature is extremely weak, whereas a clear Doppler velocity boundary is shown in Fig. 8(b). The different NRCS intensity structures above and below the image can be observed. This NRCS intensity structure may be related to the planetary boundary layer rolls that depend on air-sea temperature difference. Radar signatures observed at VV polarization are essentially influenced by variations of the wind speed and thermal stratification [9], which may account for the oceanic front signature weak in the SAR intensity image. Fig. 8(c) shows the Doppler velocity gradient with the extracted oceanic front (solid black line) overlaid on. Fig. 8(d) shows the SAR intensity image with the oceanic front extraction result superimposed.

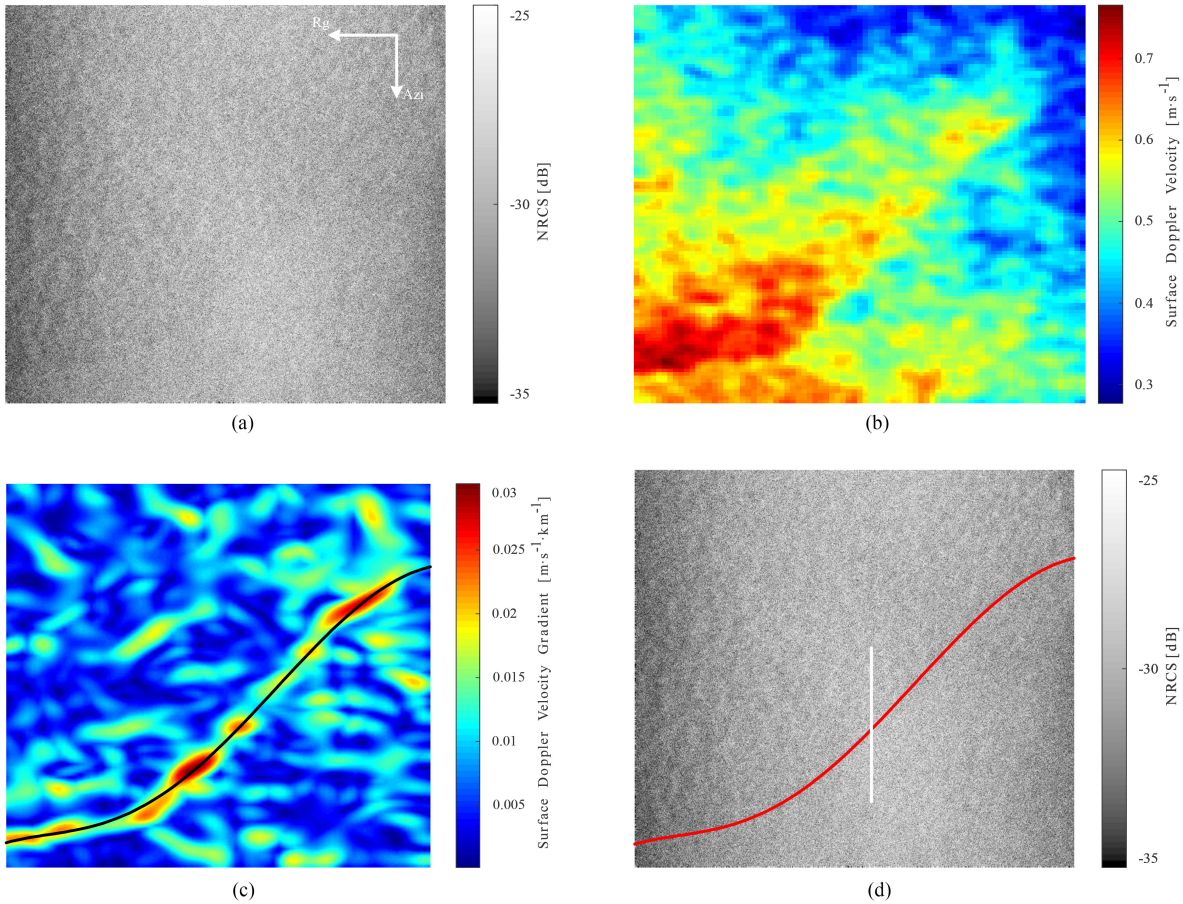


Fig. 8. Case of GF-3 FSI mode data acquired on April 26, 2021 at 21:11:54 UTC (descending pass, VV polarization). (a) SAR intensity image. The azimuth (A) and range (R) directions are indicated by arrows. (b) Estimated Doppler velocity. (c) Doppler velocity gradient with the extracted oceanic front (solid black line) superimposed. (d) Oceanic front extraction result. The solid white line indicates the transect for the analysis.

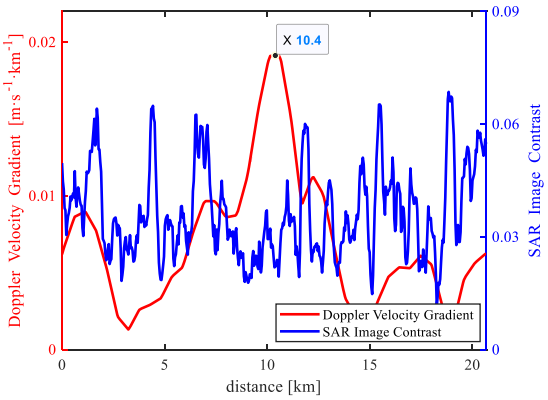


Fig. 9. Comparison of variations of SAR image contrast and the Doppler velocity gradient along the transect shown by white line in Fig. 8(d), where the red line indicates the variation of the Doppler velocity gradient along the transect, the blue line indicates the variation of SAR image contrast along the transect.

*2) Interpretation:* The SAR image contrast transect shown by the solid white line in Fig. 8(d) and its corresponding Doppler velocity gradient transect are taken. Variations of SAR image contrast and the Doppler velocity gradient along the transect are shown in Fig. 9. The variation of the Doppler velocity gradient has a highest peak located at 10.4 km along the transect, whereas the variation of SAR image contrast is relatively uniform, without a significant peak. Fig. 9 implies that the oceanic front extracted from the Doppler velocity gradient is an effective supplement in the case where the oceanic front signature is extremely weak in the SAR intensity image.

Fig. 10(a) shows the SST gradient derived from the SST data acquired on April 26, 2021 at 12:00:00 UTC, where the red box refers to the location of GF-3 image. Fig. 10(b) shows an enlarged image in the study area with the oceanic front extracted from SAR (thick black line) superimposed. As shown in Fig. 10(b), the oceanic front extracted from SAR falls within the 22.2 °C–22.4 °C isotherms with an SST gradient of approximately 0.03–0.04 °C/km. Changes in the marine atmospheric boundary layer or in the viscous properties of the sea surface induced by the spatial variations of SST [31], dynamics of local turbulent conditions and time-varying vertical mixing conditions due to fluid dynamics lead to variations in NRCS. Although the probability of change is high near SST gradients, NRCS, and Doppler changes are not exactly collocated with the steepest SST gradient. In addition, taking into account the time difference between SST and SAR data acquisition, the extraction results of oceanic fronts can be considered plausible as long as the frontal line falls within or near the frontal zone. Moreover, the

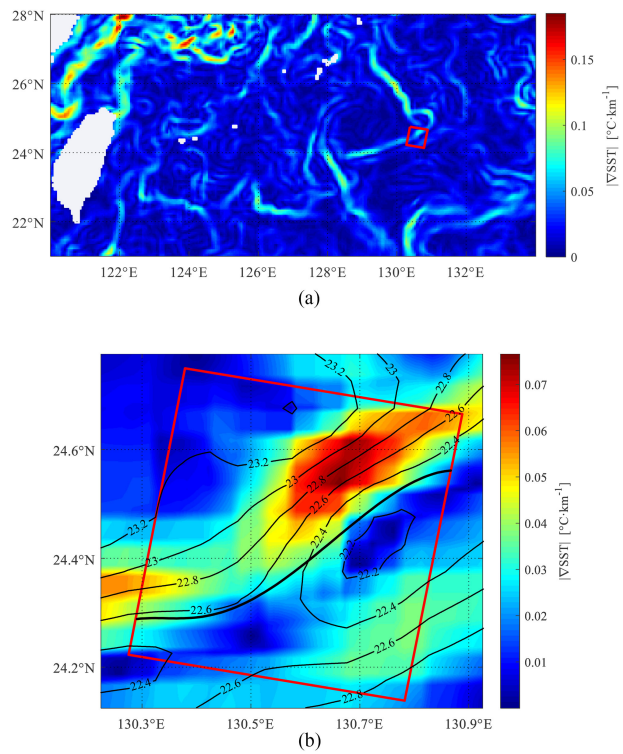


Fig. 10. (a) SST gradient derived from the SST data acquired on April 26, 2021 at 12:00:00 UTC, where the red box refers to the location of the GF-3 image. (b) An enlarged image at the location of the SAR image with the extracted oceanic fronts from SAR (thick black line) superimposed, and the overlaid thin black lines represent the isotherms.

orientation of the front extracted from SAR is consistent with the orientation of the SST gradient, which demonstrates in the case where the signature of oceanic front is extremely weak in the SAR intensity images, the oceanic front extracted from the ocean surface Doppler velocity gradient is credible.

## IV. Discussion

In this study, we extracted oceanic fronts from both the intensity and the Doppler from GF-3 SLC data. In general, VV polarized data are preferred for extracting oceanic fronts from SAR intensity images because of their high NRCS [32]. Both wind and currents affect the sea surface NRCS and thus the extraction of oceanic fronts. Winds coming toward or away from the antenna look direction have higher NRCS than winds that are offset from the antenna direction, and the surface NRCS increases with the increase of wind speed [32]. Frontal currents change the surface NRCS due to wave-current interaction. The current gradient modulates the sea surface NRCS while a constant current only affects the surface mean NRCS.

The Doppler velocity contains contributions from ocean surface motion induced by wind and the underlying ocean currents [33], [34]. Due to surface wind, the Doppler velocity for HH polarization is always larger than that for VV polarization [35]. However, the Doppler velocity gradient, rather than the precise current velocity, is of interest for oceanic front extraction. In addition, significant changes in the wind direction appears at the regions along the front [31], which further enhances the Doppler velocity gradient and makes it easier to extract the oceanic front from the Doppler velocity gradient. The Doppler velocity increases with radially directed wind and current as well as increasing wind and current velocity, and maximum Doppler velocity corresponds to cases when the wind and current are strong and parallel to the antenna look direction [33], [34]. For case in which oceanic fronts are aligned with range direction, the extraction of oceanic fronts from the Doppler velocity gradient works best.

In addition to wind and currents, the extraction of oceanic fronts is also affected by radar parameters. In future work, SAR data with different imaging modes, frequency, bands, polarizations, and incidence angles will be collected to study their effects on oceanic front extraction. In addition, oceanic front extraction under complex ocean backgrounds needs to be performed to validate the positive results obtained in this study.

## V. Conclusion

This article was aimed at extracting oceanic fronts from GF-3 SAR data, especially for the case that the oceanic front signature is not clearly visible in the SAR intensity images. A method combing intensity and Doppler information to extract oceanic fronts was proposed, which takes benefit of the high resolution of the SAR intensity images and takes benefit of the good performance of the Doppler in capturing the velocity gradient across a front. A detailed presentation of the data processing scheme for oceanic front extraction was provided. The performance of the method was verified by application to three cases that oceanic front signatures were clearly visible, partially visible, and extremely weak in the SAR intensity images. The results showed that the oceanic front extracted from the Doppler velocity gradient can not only complement the oceanic front extracted from SAR intensity images, but also can be used as a reference for the oceanic front extracted from SAR intensity images. The Doppler velocity, as supplementary information, improves the capability of oceanic front extraction from SAR data.

## Acknowledgment

The authors would like to thank the editors and the two anonymous reviewers for their constructive comments and recommendations.

## References

[1] I. M. Belkin, P. C. Cornillon, and K. Sherman, "Fronts in large marine ecosystems," *Prog. Oceanogr.*, vol. 81, no. 1–4, pp. 223–236, 2009.
[2] C. C. Wall, F. E. Muller-Karger, M. A. Roffer, C. Hu, W. Yao, and M. E. Luther, "Satellite remote sensing of surface oceanic fronts in coastal waters off west–central Florida," *Remote Sens. Environ.*, vol. 112, no. 6, pp. 2963–2976, 2008.
[3] D. R. Lyzenga, "Interaction of short surface and electromagnetic waves with ocean fronts," *J. Geophys. Res., Oceans*, vol. 96, no. C6, pp. 10765–10772, 1991.
[4] R. Romeiser, S. Ufermann, and S. Kern, "Status report on the remote sensing of current features by spaceborne synthetic aperture radar," in *Proc. 2nd Workshop Coastal Mar. Appl. SAR*, 2003, pp. 105–124.
[5] C. T. Jones, T. D. Sikora, P. W. Vachon, and J. Wolfe, "Toward automated identification of sea surface temperature front signatures in Radarsat-2 images," *J. Atmos. Ocean. Technol.*, vol. 29, no. 1, pp. 89–102, 2012.

[6] C. T. Jones, T. D. Sikora, P. W. Vachon, J. Wolfe, and B. Detracey, "Toward automated identification of sea surface temperature front signatures in Radarsat-2 images," *J. Atmos. Ocean. Technol.*, vol. 30, no. 9, pp. 2203–2215, 2013.
[7] W. Van Wychen, P. W. Vachon, J. Wolfe, and K. Biron, "Synergistic RADARSAT-2 and Sentinel-1 SAR images for ocean feature analysis," *Can. J. Remote Sens.*, vol. 45, no. 5, pp. 591–602, 2019.
[8] S. R. Chubb *et al.*, "Study of Gulf Stream features with a multifrequency polarimetric SAR from the space shuttle," *IEEE Trans. Geosci. Remote Sens.*, vol. 37, no. 5, pp. 2495–2507, Sep. 1999.
[9] S. Ufermann and R. Romeiser, "A new interpretation of multifrequency/multipolarization radar signatures of the Gulf Stream front," *J. Geophys. Res., Oceans*, vol. 104, no. C11, pp. 25697–25705, 1999.
[10] J. A. Johannessen *et al.*, "Coastal ocean fronts and eddies imaged with ERS 1 synthetic aperture radar," *J. Geophys. Res. Atmos.*, vol. 101, no. 15, pp. 6651–6667, 1996.
[11] J. A. Johannessen, V. Kudryavtsev, D. Akimov, T. Eldevik, N. Winther, and B. Chapron, "On radar imaging of current features: 2. Mesoscale eddy and current front detection," *J. Geophys. Res. Atmos.*, vol. 110, no. C7, 2005, Art. no. C07017.
[12] O. Isoguchi, N. Ebuchi, and M. Shimada, "Meso-and submeso-scale ocean front detection using SAR and optical data," in *Proc. IEEE Int. Geosci. Remote Sens. Symp.*, 2016, pp. 4043–4045.
[13] N. Allan, C. L. Trump, D. B. Trizna, and D. J. McLaughlin, "Dual-polarized Doppler radar measurements of oceanic fronts," *IEEE Trans. Geosci. Remote Sens.*, vol. 37, no. 1, pp. 395–417, Jan. 1999.
[14] P. Flament and L. Armi, "The shear, convergence, and thermohaline structure of a front," *J. Phys. Oceanogr.*, vol. 30, no. 1, pp. 51–66, 2000.
[15] N. Rascle *et al.*, "Monitoring intense oceanic fronts using sea surface roughness: Satellite, airplane, and in situ comparison," *J. Geophys. Res., Oceans*, vol. 125, no. 8, 2020, Art. no. e2019JC015704.
[16] B. Chapron, F. Collard, and F. Ardhuin, "Direct measurements of ocean surface velocity from space: Interpretation and validation," *J. Geophys. Res.*, vol. 110, no. C7, 2005, Art. no. C07008.
[17] J. A. Johannessen *et al.*, "Direct ocean surface velocity measurements from space: Improved quantitative interpretation of Envisat ASAR observations," *Geophys. Res. Lett.*, vol. 35, no. 22, 2008, Art. no. L22608.
[18] K. Biron, W. Van Wychen, and P. W. Vachon, "Gulf stream detection from SAR Doppler anomaly," *Can. J. Remote Sens.*, vol. 44, no. 4, pp. 311–320, 2019.
[19] I. G. Cumming and F. H. Wong, *Digital Processing of Synthetic Aperture Radar Data Algorithms and Implementation*. Norwood, MA, USA: Artech House, 2005.
[20] M. I. Skolnik, *Radar Handbook*, 3rd ed. New York, NY, USA: McGraw-Hill, 2008.
[21] M. W. Hansen, F. Collard, K. Dagestad, J. A. Johannessen, P. Fabry, and B. Chapron, "Retrieval of sea surface range velocities from Envisat ASAR Doppler centroid measurements," *IEEE Trans. Geosci. Remote Sens.*, vol. 49, no. 10, pp. 3582–3592, Oct. 2011.
[22] S. N. Madsen, "Estimating the Doppler centroid of SAR data," *IEEE Trans. Aerosp. Electron. Syst.*, vol. 25, no. 2, pp. 134–140, Mar. 1989.
[23] R. Bamler and H. Runge, "PRF-ambiguity resolving by wavelength diversity," *IEEE Trans. Geosci. Remote Sens.*, vol. 29, no. 6, pp. 997–1003, Nov. 1991.
[24] R. K. Raney, "Doppler properties of radars in circular orbits," *Int. J. Remote Sens.*, vol. 7, no. 9, pp. 1153–1162, 2007.
[25] X. M. Li, T. Y. Zhang, B. Q. Huang, and T. Jia, "Capabilities of Chinese Gaofen-3 synthetic aperture radar in selected topics for coastal and ocean observations," *Remote Sens.*, vol. 10, no. 12, 2018, Art. no. 1929.
[26] L. Ren *et al.*, "Assessments of ocean wind retrieval schemes used for Chinese Gaofen-3 synthetic aperture radar co-polarized data," *IEEE Trans. Geosci. Remote Sens.*, vol. 57, no. 9, pp. 7075–7085, Sep. 2019.
[27] L. Ren *et al.*, "Preliminary analysis of Chinese GF-3 SAR quad-polarization measurements to extract winds in each polarization," *Remote Sens.*, vol. 9, no. 12, 2017, Art. no. 1215.
[28] H. Wang *et al.*, "Empirical algorithm for significant wave height retrieval from wave mode data provided by the Chinese satellite Gaofen-3," *Remote Sens.*, vol. 10, no. 3, 2018, Art. no. 363.
[29] X. F. Li, C. Y. Li, W. G. Pichel, P. Clernente-Colón, and K. S. Friedman, "Synthetic aperture radar imaging of axial convergence fronts in Cook Inlet, Alaska," *IEEE J. Ocean. Eng.*, vol. 30, no. 3, pp. 543–551, Jul. 2005.
[30] C. J. Donlon, M. J. Martin, J. Stark, J. Roberts-Jones, E. Fiedler, and W. Wimmer, "The operational sea surface temperature and sea ice analysis (OSTIA) system," *Remote Sens. Environ.*, vol. 116, pp. 140–158, 2012.
[31] T. -S. Kim, K. -A. Park, X. Li, A. A. Mouche, B. Chapron, and M. Lee, "Observation of wind direction change on the sea surface temperature front using high-resolution full polarimetric SAR data," *IEEE J. Sel. Topics Appl. Earth Observ. Remote Sens.*, vol. 10, no. 6, pp. 2599–2607, Jun. 2017.
[32] C. R. Jackson and J. R. Apel, *Synthetic Aperture Radar: Marine User's Manual*. Camp Springs, MY, USA: Nat. Ocean. Atmospher. Admin., 2004.
[33] A. Moiseev, H. Johnsen, M. Hansen, and J. Johannessen, "Evaluation of radial ocean surface currents derived from Sentinel-1 IW Doppler shift using coastal radar and Lagrangian surface drifter observations," *J. Geophys. Res., Oceans*, vol. 125, no. 4, 2020, Art. no. e2019JC015743.
[34] A. Moiseev, H. Johnsen, J. A. Johannessen, F. Collard, and G. Guitton, "On removal of sea state contribution to Sentinel-1 Doppler shift for retrieving reliable ocean surface current," *J. Geophys. Res.: Oceans*, vol. 125, no. 9, 2020, Art. no. C07008.
[35] A. A. Mouche *et al.*, "On the use of Doppler shift for sea surface wind retrieval from SAR," *IEEE Trans. Geosci. Remote Sens.*, vol. 50, no. 7, pp. 2901–2909, Jul. 2012.

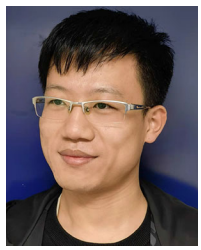

**Kai Sun** received the B.S. degree in electronic engineering from Dalian Maritime University, Dalian, China, in 2018. He is currently working toward the Ph.D. degree in signal and information processing with the Aerospace Information Research Institute, Chinese Academy of Sciences and the University of Chinese Academy of Sciences, Beijing, China.

His research interests include signal processing, theory and applications of SAR in ocean remote sensing.

**Jinsong Chong** (Senior Member, IEEE) received the B.S. degree from Jilin University, Changchun, China, in 1991, the M.S. degree from the Beijing University of Aeronautics and Astronautics, Beijing, China, in 2000, and the Ph.D. degree from the Graduate School, Chinese Academy of Sciences, Beijing, in 2003.

She was a Visiting Scholar with Monash University, Melbourne, Australia, in 2004. She was a Tan Chin Tuan Exchange Fellow with Nanyang Technological University, Singapore, in 2005. She is currently a Research Professor with the Aerospace Information Research Institute, Chinese Academy of Sciences. Her research interest focuses on microwave remote sensing of ocean.

**Lijie Diao** received the B.S. degree in communication engineering from Shandong University, Qingdao, China, in 2021. She is currently working toward the Ph.D. degree in signal and information processing with the Aerospace Information Research Institute, Chinese Academy of Sciences and the University of Chinese Academy of Sciences, Beijing, China.

Her research interest includes microwave remote sensing of the ocean.

**Zongze Li** received the B.S. degree in communication engineering from Jilin University, Changchun, China, in 2020. She is currently working toward the Ph.D. degree in signal and information processing with the Aerospace Information Research Institute, Chinese Academy of Sciences and the University of Chinese Academy of Sciences, Beijing, China.

Her research interests include microwave ocean remote sensing and image information processing.

**Xianen Wei** received the B.S. degree in communication engineering from Dalian Maritime University, Dalian, China, in 2020. He is currently working toward the Ph.D. degree in signal and information processing with the Aerospace Information Research Institute, Chinese Academy of Sciences and the University of Chinese Academy of Sciences, Beijing, China.

His research interest includes microwave remote sensing of the ocean.